

Optical readout of a superconducting qubit using a piezo-optomechanical transducer

In the format provided by the
authors and unedited

SUPPLEMENTARY INFORMATION

Optical readout of a superconducting qubit using a piezo-optomechanical transducer

T.C. van Thiel,¹ M.J. Weaver,¹ F. Berto,¹ P. Duivestein,¹ M. Lemang,¹ K.L. Schuurman,¹ M. Žemlička,¹ F. Hijazi,¹ A.C. Bernasconi,¹ C. Ferrer,¹ E. Cataldo,¹ E. Lachman,² M. Field,² Y. Mohan,² F.K. de Vries,³ C.C. Bultink,³ J. van Oven,³ J.Y. Mutus,² R. Stockill,^{1,*} and S. Gröblacher^{1,†}

¹*QphoX B.V., Elektronicaweg 10, 2628XG, Delft, The Netherlands*

²*Rigetti Computing Inc., 775 Heinz Avenue,
Berkeley, California, 94710, United States*

³*Qblox B.V., Delftchpark 22, 2628XH, Delft, The Netherlands*

(Dated: January 6, 2025)

CONTENTS

I. Fabrication	2
II. Transducer characterization	3
III. Added noise	7
A. Thermal noise	7
B. Shot noise	10
IV. Pump induced decoherence	13
V. Experimental setup	16
References	16

* rob@qphox.eu

† simon@qphox.eu

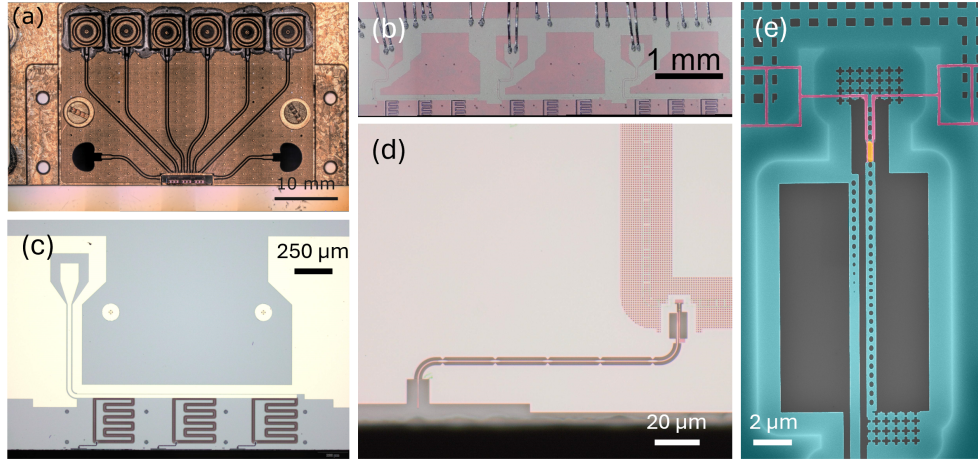


FIG. S1. Integrated piezo-optomechanical transducer. Optical microscope images of (a) the chip carrier with a mounted transducer chip, (b) the transducer chip with wirebonds to the chip carrier SMP electrical ports, (c) three electrically multiplexed transducer devices coupled to a microwave transmission line in a hanger geometry, (d) the transducer optical waveguide edge coupler and (e) a SEM image of a representative transducer device.

I. FABRICATION

The starting material for these devices is a 330 nm film of X-cut LiNbO₃ (LN) bonded on an high resistivity silicon on insulator (SOI) substrate. The full device fabrication consists of four main parts. In the first one, an Ar milling process is patterning the LN layer to form small blocks. The second one involves the formation of the nanobeams using a reactive-ion etch (RIE) step. Afterwards, a deposition of a 45 nm thick MoRe layer fabricates the bondpads, the feedline, and the resonators. Finally, a buffered oxide etch (BOE) solution selectively etches the sacrificial SiO₂ layer underneath the Si device layer to suspend the devices. This step enables the oxide under the resonators to be removed and thus to increase the electrical quality factor of the devices. Further details regarding the fabrication is described in previous work [1].

After fabrication, samples are mounted on top of a copper chip carrier using GE varnish and the transducer microwave ports are wire bonded to electrical lines ending in soldered SMP connectors (Figs. S1a-b). Each microwave transmission line electrically multiplexes three transducer devices in hanger geometry in reflection (Fig. S1c). The optical port of the transducer device consists of a waveguide edge coupler at the edge of the chip, which can

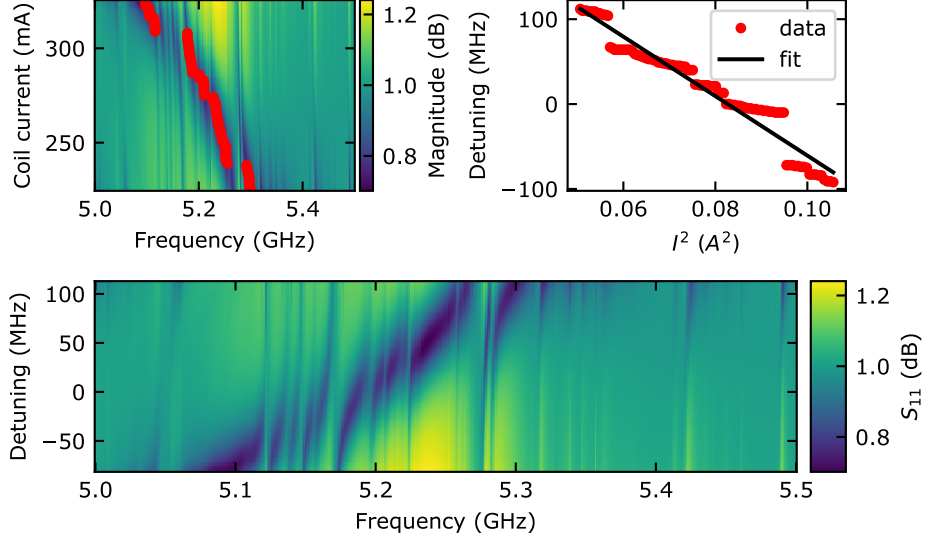


FIG. S2. Tuning of the microwave resonance. (a) Microwave reflection spectrum as for different coil currents and probe frequencies. The red dots indicate the microwave resonance dip. (b) Microwave resonance as a function of the square of the coil current with a linear fit. (c) Microwave reflection spectrum as a function of probe frequency and resonance detuning.

be coupled to with a lensed fiber (Fig. S1d). A SEM image of a representative transducer device is shown in (Fig. S1e).

II. TRANSDUCER CHARACTERIZATION

The (side-coupled) transducer microwave resonator consists of a 160 nm wide superconducting wire, organized into a half-wave laddered comb-like loop. The ladder subloops combined with the high kinetic inductance (around 10 pH/square) of the MoRe superconducting layer allow for tuning of the resonance frequency, as described in ref. [2]. An external superconducting coil is mounted in close proximity to the transducer chip, yielding a field-to-current ratio of about 10 mT A^{-1} at the sample. This leads to a tunability of typically several hundreds of MHz and facilitates bringing the microwave resonator into resonance with the transducer optomechanically-active electromechanical mechanical mode. Fig. S2 illustrates tuning of the microwave resonance through several electromechanical modes.

Fig. S3 shows the electrical, mechanical and optical resonances of the piezo-optomechanical system. To determine the external and internal electrical coupling rates, the microwave res-

TABLE I. Device and experimental parameters.

Parameter Name	Description	Value	Error	Units
Transducer Property				
$\omega_m/2\pi$	mechanical resonance frequency	5.19442		GHz
$\omega_o/2\pi$	optical resonance frequency	191.57		THz
$\omega_p/2\pi$	frequency of peak conversion efficiency	5.198		GHz
$\kappa_m/2\pi$	mechanical linewidth	1.53	0.01	MHz
$\kappa_e/2\pi$	total microwave loss rate	23.6	5.32	MHz
$\kappa_{ee}/2\pi$	microwave external coupling rate	12.2	2.84	MHz
$\kappa_{ei}/2\pi$	microwave internal loss rate	11.4	2.48	MHz
$\kappa_o/2\pi$	total optical loss rate	5.16	0.03	GHz
$\eta_e \equiv \frac{\kappa_{ee}}{\kappa_e}$	microwave resonator coupling	0.517	0.08	
$\eta_o \equiv \frac{\kappa_{oe}}{\kappa_o}$	optical resonator coupling	0.5	0.18	
Qubit Property				
$\omega_r/2\pi$	bare readout resonator frequency	5.194		GHz
$\omega'_r/2\pi$	dressed readout resonator frequency	5.198		GHz
$\omega_q/2\pi$	qubit frequency	4.07		GHz
$\kappa_{re}/2\pi$	readout resonator linewidth	500		kHz
$\kappa_{ree}/2\pi$	readout resonator external coupling rate	450		kHz
$\kappa_{ree}/2\pi$	readout resonator internal coupling rate	50		kHz
$g/2\pi$	qubit-resonator coupling	52	0.1	MHz
$\chi/2\pi$	dispersive shift	512	20	kHz
Experimental Setup Property				
η_{fiber}	fiber coupling efficiency	0.40	0.01	
η_{od}	optical output detection efficiency	0.43	0.05	
η_{tod}	total optical detection efficiency	0.17	0.05	

onator is detuned from any electromechanical modes and its transmission spectrum is fit following the routine described in ref. [3] (see Fig. S3a). We find internal and external coupling rates of 11.4 MHz and 12.2 MHz, respectively i.e., an overcoupled resonator with a (side-)coupling coefficient of $\eta_e = 0.517$. The mechanical resonance of the optomechanical

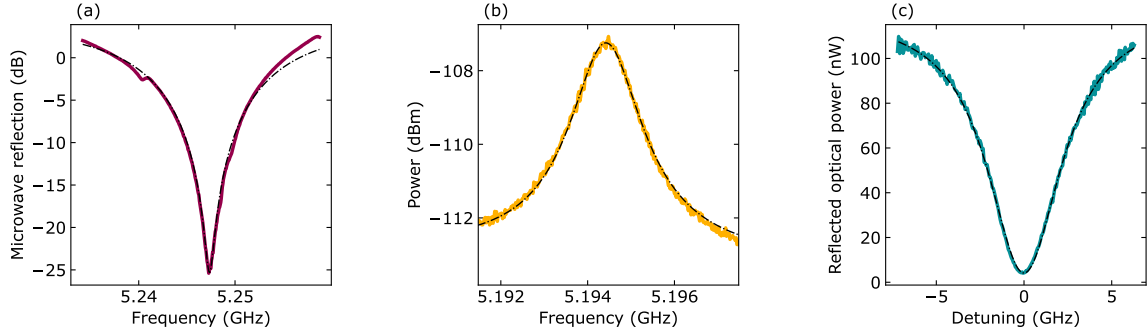


FIG. S3. Resonances of the piezo-optomechanical transducer. (a) Microwave resonance with the magnetic field set to a detuning far away from any electromechanically active mechanical modes. (b) Thermal modulation of the optical frequency due to the optomechanically active mechanical mode, measured through optical heterodyne detection. (c) Reflection measurement of the optical resonance of the photonic crystal cavity.

cavity is determined at 4 K, where it exhibits ample thermal motion. The GHz modulation of the hundreds of THz optical resonance by the thermally-excited mechanical mode is extracted through optical heterodyne detection, using a high-speed photodetector. The result is shown in Fig. S3b. We fit the data with a Lorentzian function, which yields a resonance frequency of $\omega_m/2\pi = 5.194\ 42\ \text{GHz}$ with a total linewidth of $\kappa_m/2\pi = 1.53\ \text{MHz}$. Note that, due to hybridization with the electromechanical mode of the LiNbO₃ piezoelectric block, the frequency of peak transduction efficiency ($\omega_p/2\pi = 5.198\ \text{GHz}$) is slightly shifted from the mechanical resonance. Fig. S3c shows the optical cavity response, exhibiting a frequency of $\omega_o/2\pi = 191.57\ \text{THz}$, linewidth of $\kappa_o/2\pi = 5.16\ \text{GHz}$ and waveguide-to-resonator coupling efficiency of $\eta_o \approx 0.5$, with a fiber-to-waveguide coupling of $\eta_{fiber} = 0.4$. The results are summarized in Table I.

Following the approach of ref. [4], we characterize the transducer conversion efficiency with a four-port vector network analyzer (VNA) measurement. Upconversion is measured by applying a continuous microwave tone to the transducer electrical input port and demodulating the transduced optical signal using a heterodyne scheme incorporating a fast photodetector. The resulting microwave signal is collected by one of the two VNA input ports. Downconversion is measured through application of a microwave tone to an electro-optic modulator (EOM), generating optical sidebands on the red-detuned optical pump directed towards the optical input of the transducer. The transducer demodulates the com-

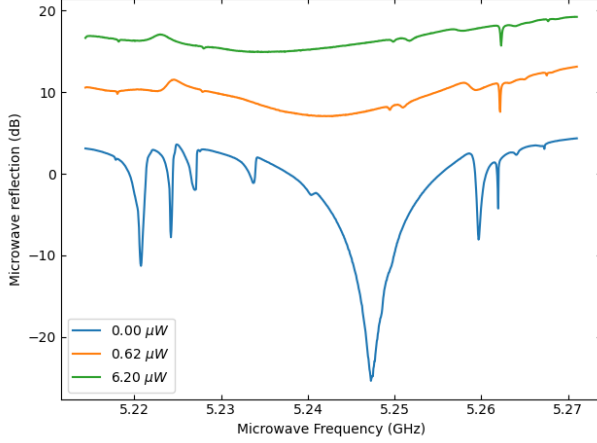


FIG. S4. Optical effect on the transducer microwave resonator. Microwave resonance of the transducer measured in reflection with (blue) no optical pump power, (orange) $0.62 \mu\text{W}$ of optical pump power and (green) $6.2 \mu\text{W}$ of optical pump power. Curves are offset vertically for clarity

posite optical signal to the microwave domain. The signal is subsequently amplified by 4 K HEMT and room-temperature low-noise amplifiers and collected by the other VNA input port. The transduction efficiency is calculated as

$$\eta = 2\alpha \frac{|S_{eo}||S_{oe}|}{|S_{ee}||S_{oo}|}, \quad (1)$$

where S_{eo} (S_{oe}) is the upconversion (downconversion) and S_{ee} (S_{oo}) is the reflected microwave (optical) signal. The term $2\alpha \approx 1.3$ corrects for a nonzero rejection of the lower optical sideband. The data reported here was recorded with a phase EOM, with the correction to the efficiency values calibrated by a subsequent amplitude EOM transduction measurement.

In the same way as we observed in reference [1], the optical field required to operate the transducer results in an increase loss rate of the superconducting microwave resonator, as well as a reduction of the resonator frequency. Figure S4 displays the reflected microwave power around the microwave resonator under increasing optical power input into the system. The data are taken for an pump red-detuned from the optical resonance by 5.2 GHz, as used for the transducer characterization and qubit readout in the main text.

Fig. S5 illustrates the impact of the optical pump on the phase response of the optical readout system. The phase space statistical distributions of the single-shot readout experi-

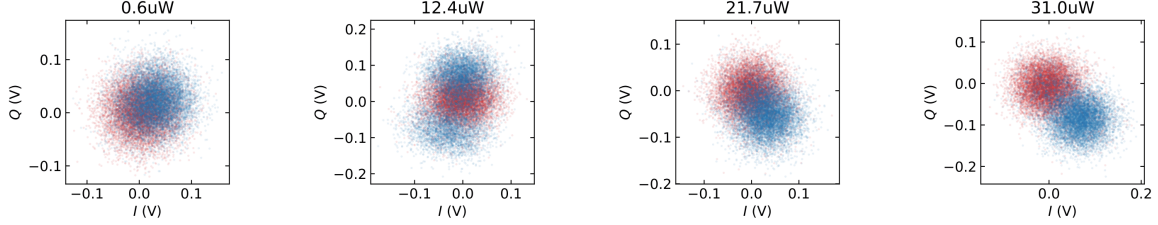


FIG. S5. Optically-dependent readout phase shift. Single-shot optical readout statistical distributions for various optical powers with (red) the $|1\rangle$ state and (blue) the $|0\rangle$ state prepared.

ments exhibit a phase shift with high optical powers. At the transition between low and high powers at 12.4 uW the system is unstable and jumps between two positions in phase space. This explains the low fidelity at this power in Fig. 3c of the main text. We attribute this phase shift to the previously observed dependence of the transducer microwave resonator amplitude and phase response on optical pump power [1].

III. ADDED NOISE

In the main text we report added noise, which is the noise referred to the beginning of the microwave field detection path, immediately after the qubit readout resonator. Laser amplitude fluctuations are mitigated by a balanced heterodyne scheme, which largely suppresses (~ 40 dB) any common mode noise between the signal and local-oscillator optical paths. The overall noise floor is dominated by Poissonian shot noise of the powerful local oscillator (~ 1 mW), which amplifies the coherent tones from the signal input port and adds shot noise, both proportional to the square root of the optical power. The input-referred added noise therefore, is mainly determined by the transduction efficiency and the optical detection efficiency in the signal path. The two main noise contributions in our experimental setup are thermal noise in the transducer mechanical resonator and optical heterodyne shot noise. In the following sections we briefly discuss the extraction of these two quantities.

A. Thermal noise

The optical power resulting from the upconversion of a given microwave input power $P_{e,in}$ is given by

$$P_{o,sig} = \frac{\omega_o}{\omega_e} \eta_t \eta_c P_{e,in}, \quad (2)$$

with ω_e (ω_o) the microwave (optical) angular frequency, η_t the photon conversion efficiency and η_c the optical collection efficiency, comprising optical losses along the chain, as well as the quantum efficiency of the photodetector. Thermal noise power added by the mechanical resonator $P_{m,th}$ appears on the output as

$$P_{o,th} = \frac{\omega_o}{\omega_m} \eta_{om} \eta_{em} P_{m,th} = \frac{\omega_o}{\omega_m} \eta_t \eta_c P_{e,th}, \quad (3)$$

where we use the relation $\eta_t = \eta_{om} \eta_{em}$, with η_{om} (η_{em}) the optomechanical (electromechanical) conversion efficiency. The optical signal-to-thermal-noise ratio is then given by

$$\text{SNR}_o = \frac{\omega_m}{\omega_e} \frac{P_{e,in}}{P_{e,th}} \approx \frac{P_{e,in}}{P_{e,th}}, \quad (4)$$

with ω_m the mechanical resonance frequency and $P_{e,th}$ the input-referred thermal noise power. In a heterodyne scheme, the measured signal-to-noise ratio on a photodiode output is linearly proportional to the optical signal-to-noise ratio on the input. We then have for the thermal noise equivalent power

$$P_{e,th} = \frac{P_{e,in}}{\text{SNR}_{meas}}, \quad (5)$$

which is in general a frequency dependent property due to the resonant nature of the thermal noise. Accordingly, the added noise in an experiment depends sensitively on the microwave signal and mechanical resonance frequencies, with the thermal noise being smaller or even negligible when they differ and maximum when they are equal.

To determine the microwave power on the input of the transducer microwave port, we make use of the AC Stark shift effect, which leads to a readout power-dependent frequency shift of the qubit given by $\Delta\nu = 2\bar{n}\chi$, with χ the dispersive shift [5] and \bar{n} the intracavity photon number of the readout resonator. Figure S6a shows the readout resonator response for the qubit prepared in the $|0\rangle$ and $|1\rangle$ states, revealing a dispersive shift of $\chi/2\pi = 512$ kHz.

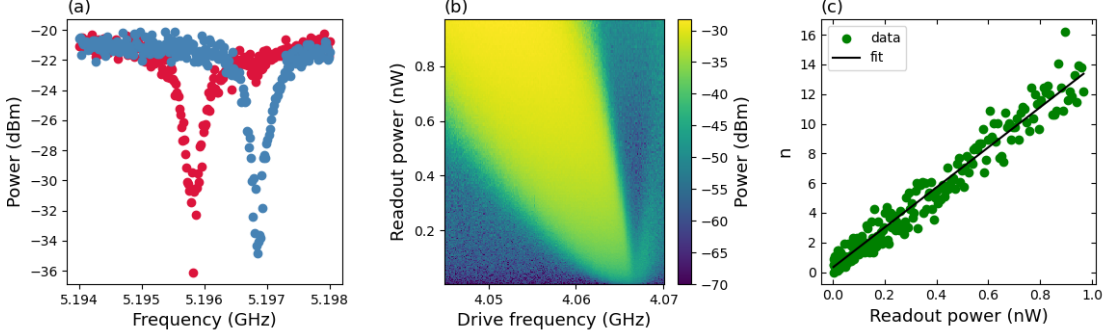


FIG. S6. Line attenuation. Panel (a) shows the readout resonator response with the qubit prepared in the (blue) $|0\rangle$ state and (red) $|1\rangle$ state, from which we extract a dispersive shift $\chi/2\pi = 512$ kHz. Panel (b) depicts two-tone spectroscopy data as a function of room temperature readout power and qubit drive frequency for fixed qubit drive power. The data shows the Stark shift of the qubit frequency due to an increase in the intracavity photon number of the readout resonator. The extracted photon number as a function of room temperature readout power is shown in panel (c).

If the readout resonator is driven on resonance, the intracavity photon number is given by [6, 7]

$$\bar{n} = \frac{4}{\hbar\omega_0} \frac{\kappa_{ext}}{\kappa_{tot}^2} P_{e,in} = \frac{4}{\hbar\omega_0} \frac{\kappa_{ext}}{\kappa_{tot}^2} \alpha P_{e,rt}, \quad (6)$$

with κ_{tot} (κ_{ext}) the total (external) loss rate of the readout resonator, ω_0 the unshifted dressed readout resonator frequency, α the cryogenic line attenuation and $P_{e,rt}$ the microwave power applied at room temperature. The qubit frequency as a function of readout power is determined by two-tone spectroscopy (see Fig. S6b). From the power-dependent frequency shift, we determine the intracavity photon number \bar{n} as a function of the microwave readout power applied at room temperature (see Fig. S6c). With the readout resonator loss rates $\kappa_{ext}/2\pi = 0.45$ MHz and $\kappa_{tot}/2\pi = 0.5$ MHz, we extract an attenuation of 73.8 dB. We estimate the total line attenuation to be $74.5 \text{ dB} \pm 0.5 \text{ dB}$ due to additional insertion losses of circulators and connectors between the qubit readout line and the transducer microwave port.

We determine the thermally added noise by measuring simultaneously the upconverted

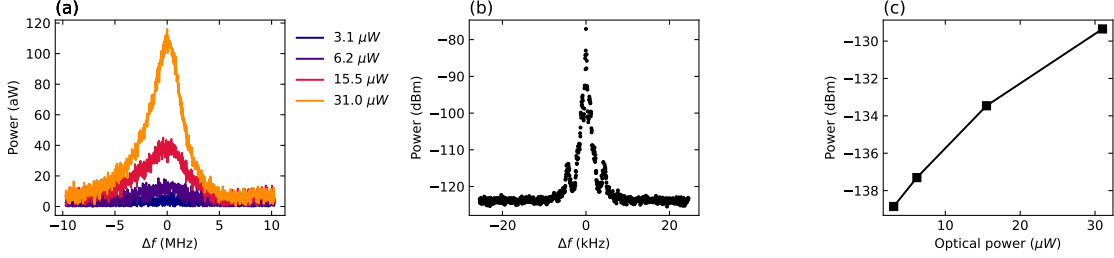


FIG. S7. **Thermal noise.** (a) Background corrected resonant thermal noise spectra measured for different optical powers. (b) Upconverted microwave tone at 15.5 μW of optical power. (c) Thermal noise power as a function of optical power.

signal of applied microwave tone and thermal phonons in the optomechanical resonator at 15.5 μW of applied pump power (see Fig. S7a) using heterodyne detection. Correcting for non-thermal background noise sources and assuming a Lorentzian line shape of the thermal noise, we extract an average power value of -133.7 dBm over a bandwidth of 1.5 MHz. To determine the thermal noise equivalent power, we extract the signal-to-noise ratio on the photodiode output between the upconverted microwave calibration tone and the thermal noise contribution, yielding a value of 56.7 dB. From the power measured at room temperature (-22.7 dBm) and the determined line attenuation (74.5 dB), we determine the power of the microwave tone at the transducer input port to be -97.2 dBm , leading to a thermal noise equivalent power of -153.9 dBm , approximately five orders of magnitude smaller than the instantaneous microwave power used during readout. The thermal noise contributions for other optical powers is straightforwardly determined by taking the calibrated value as a reference and correcting for any measured increase/decrease in thermal noise power by the increased/decreased conversion efficiency.

B. Shot noise

The current generated by a photodiode from incident light is given by

$$i = \frac{e\eta_q}{\hbar\omega_o} P_o, \quad (7)$$

with P_o the incident optical power, e the elementary charge, ω_o the optical frequency and η_q the quantum efficiency of the detector. The generated electrical noise power is

$$\delta P_e = Z \text{Var}(i) = Z \left(\frac{e\eta_q}{\hbar\omega_o} \right)^2 \text{Var}(P_o), \quad (8)$$

with Z the output impedance of the photodiode. The number of photons n arriving on the detector in a time interval Δt obeys Poissonian statistics $\text{Var}(n) = \bar{n}$, which in terms of the incident optical power yields

$$\text{Var}(P_o) = \frac{\hbar\omega_o}{\Delta t} \bar{P}_o. \quad (9)$$

Substituting (9) into (8) yields

$$\delta P_e \Delta t = Z \frac{e^2 \eta_q^2}{\hbar\omega_o} \bar{P}_o. \quad (10)$$

For an acquisition window of duration Δt we have for the the acquisition bandwidth $\Delta f \approx 1/\pi\Delta t$, such that

$$\delta P_e \approx 2\pi Z \frac{e^2 \eta_q^2}{\hbar\omega_o} \bar{P}_o \Delta f, \quad (11)$$

where we include a factor of two to ensure that the contributions from both the positive and negative frequency components are taken into account. To express equation 11 in terms of added noise, we divide by all the amplifications in the signal chain. In our heterodyne scheme, the measured signal is the mixed term of the upconverted transducer microwave input (P_i) with the lower sideband of the LO modulated by a phase EOM (αP_{LO}). For a phase EOM at the optimal modulation depth β , the factor α is given by the square of the maximum value of the first order Bessel function, divided by two (to only consider one sideband) $|J_1(\beta)|^2/2 \approx 0.17$ [8]. We can then write the electrical signal measured on the spectrum analyzer P_e in function of the transducer microwave input P_i

$$\begin{aligned} \bar{P}_e &= Z \left(\frac{e\eta_q}{\hbar\omega_o} \bar{P}_o \right)^2 \\ &= Z \left(\frac{e\eta_q}{\hbar\omega_o} \sqrt{\alpha \bar{P}_{LO} \bar{P}_s} \right)^2 \\ &= Z \left(\frac{e\eta_q}{\hbar\omega_o} \right)^2 \alpha \bar{P}_{LO} \eta_c \eta_t \frac{\omega_o}{\omega_e} \bar{P}_i \end{aligned} \quad (12)$$

We can now revert equation (12) to find an equation for the transducer microwave input P_i that would lead to the a power P_e measured on the spectrum analyzer

$$P_i = \frac{P_e}{Z \frac{e^2 \eta_q^2}{\hbar^2 \omega_o \omega_e} \alpha \bar{P}_{LO} \eta_c \eta_t}. \quad (13)$$

We can now define the added noise δP_{add} as the amount of noise on the transducer input that would generate a noise δP_e on the spectrum analyzer

$$\delta P_{add} = \frac{\delta P_e}{Z \frac{e^2 \eta_q^2}{\hbar^2 \omega_o \omega_e} \alpha \bar{P}_{LO} \eta_c \eta_t}. \quad (14)$$

Substituting (11) into (14) then gives the input referred shot noise

$$\delta P_{add} = \frac{2\pi \hbar \omega_e}{\alpha \eta_c \eta_t} \frac{\bar{P}_o}{\bar{P}_{LO}} \Delta f \approx \frac{2\pi \hbar \omega_e \Delta f}{\alpha \eta_c \eta_t} \quad (15)$$

Where, in the last step, we have used the fact that the power of the local oscillator is much larger than all the other powers in the experiment in a heterodyne scheme. We can now divide by the microwave photon energy $\hbar \omega_e$ in an interval of time $\Delta t = 1/\pi \Delta f$ to get the number of added noise photons on the input of the transducer

$$n_{add} \approx \frac{2}{\alpha \eta_c \eta_t} \quad (16)$$

Fig. S8 shows the heterodyne shot noise contribution to the added noise as a function of optical power for the device discussed in the main text. According to expectation, the heterodyne contribution decreases with optical power due to the increasing conversion efficiency, reducing from $\sim 1 \times 10^5$ photons to $\sim 2 \times 10^3$ photons between 0.6 μW and 31 μW optical power. We note that this contribution can be reduced or even fully removed by filtering out the portion of the local oscillator that is not amplifying the signal, increasing α in equation (16). As discussed previously, we find the added thermal contribution to the added noise to be approximately five orders of magnitude smaller than the instantaneous readout power (see Fig. S8). Accordingly, neither of these two contributions can fully explain the noise level observed in the main text. This leaves the possibility of an additional

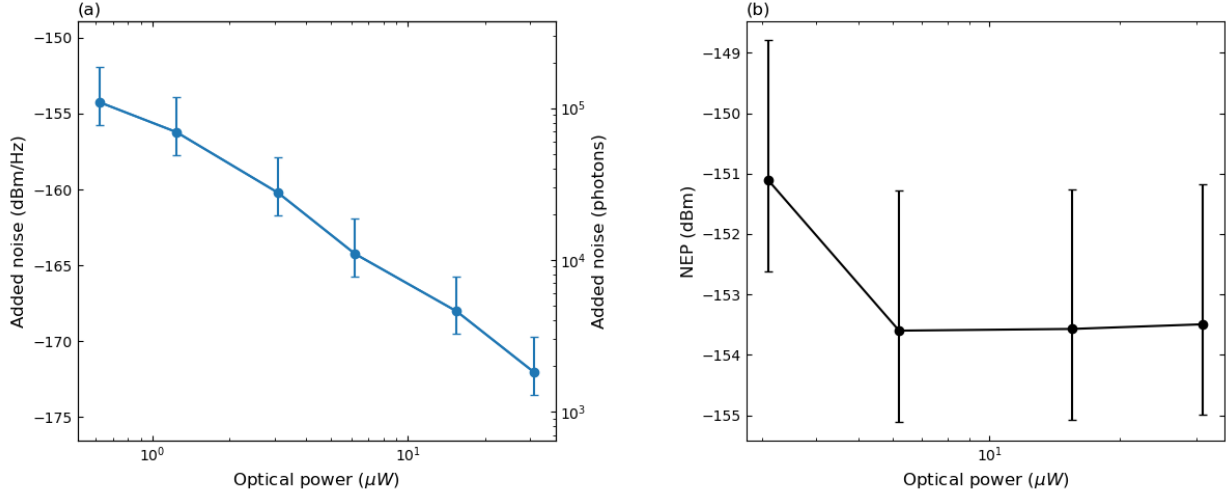


FIG. S8. **Added noise.** (a) Transducer input-referred added noise levels due to heterodyne shot noise in units of dBm/Hz (left axis) and photons (right axis) as a function of optical pump power. (b) Noise equivalent thermal power as a function of optical pump power.

contribution from the pump shot noise, which could introduce uncertainty in the number of photons in the optical cavity, thereby increasing the observed noise. However, further investigation is required to confirm the extent of this effect. A method for mitigating the pump shot noise is to improve the transducer performance to reach high levels of efficiency at lower levels of optical power.

IV. PUMP INDUCED DECOHERENCE

In the main text we demonstrate that the optical pump from the transducer does not cause measurable decoherence of the qubit with three 20 dB isolators between the transducer and the qubit. However, the necessity of adding a large number of isolators or filters might strain cryogenic space and thermal budgets, even in multiplexed optical readout scenarios. We therefore also include here data from a separate cooldown with a different transducer and characterize qubit longitudinal and transverse decay times by measuring T_1 and T_2^* with only a single 20 dB isolator inserted between the transducer and qubit readout resonator. The transducer microwave transmission output is sent to a HEMT microwave amplifier at 4K and used to determine the T_1 and T_2^* decay times using microwave-only readout, comparing scenarios with the pump continuously on or off. To obtain a robust estimation, we perform

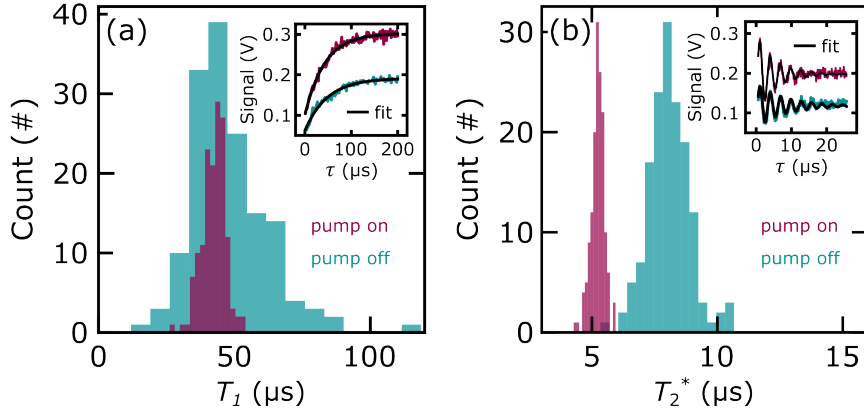


FIG. S9. Pump-induced decoherence. In a separate cooldown with a different transducer we repeat the decoherence measurements to determine the effect on the qubit with only one isolator. (a) Statistical distributions of 150 T_1 measurements, comparing the decay times with the optical pump on (purple) and off (cyan) (42.4(44) μs versus 48.1(141) μs , respectively). The inset shows two example T_1 decay curves, with fits denoted by the black lines. Similarly, panel (b) compares the statistical distributions of 150 T_2^* measurements with the pump on (purple) and off (cyan) (5.2(2) μs , versus 8.1(8) μs , respectively), with the inset showing two examples of fitted curves.

150 measurements for each scenario. Fig. S9a shows the distribution of the extracted T_1 times, with an inset illustrating two example curves and corresponding fits. We find a (statistically insignificant) reduction in mean T_1 from (pump off) 48.1 μs with a standard deviation of 14.1 μs to (pump on) 42.4 μs with a standard deviation of 4.4 μs . The difference in signal amplitude between the two scenarios, shown in the inset, can be attributed to a dependence of the transducer microwave resonator transmission on the optical pump power, which exhibits larger transmission with the optical pump on. The increased transmission has previously been shown to originate from the optical field inside the photonic cavity [1].

We further assess the impact of the pump on the transverse decay rate by measuring T_2^* . Fig. S9b shows the statistical distribution of 150 measurements, with the inset illustrating two example traces. We find a statistically significant reduction in T_2^* from (pump off) 8.1 μs with a standard deviation of 0.8 μs to (pump on) 5.2 μs with a standard deviation of 0.2 μs . We note that in the main text we operate the readout with a pulsed optical transducer pump where the optical power is turned off during the delay time of the decay time measurement. With such a pulsed operation we expect the transverse decay time to be longer even with a

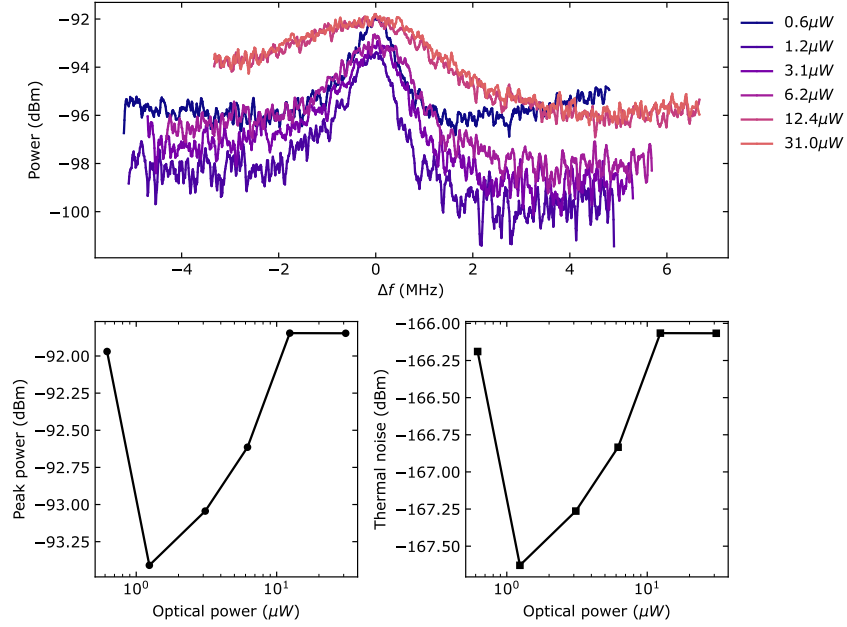


FIG. S10. **Microwave thermal noise.** (a) Thermal microwave emission spectra for different optical powers. (b) Peak thermal microwave power as a function of optical power. (c) Extracted thermal microwave emission at the transducer microwave port.

single isolator.

One interesting feature we observe in the data is that the standard deviation of the T_1 and T_2^* is decreased with the optical pump on. The reduction in variance could potentially be related to pump-induced thermal excitation of two-level systems in the qubit environment [9]. To investigate this, we directly measure the microwave emission from the transducer in the main text. We tune the transducer to its point of peak transduction efficiency and vary the optical pump power. The resulting heating of the mechanical mode leads to thermal microwave photons being emitted via the electromechanical interaction. The resulting microwave signal is subsequently amplified with a travelling-wave parametric amplifier (TWPA), as the first element in the chain and recorded with a spectrum analyser (see Figs. S10a-b). A microwave calibration tone is simultaneously inserted, which is processed by the same amplifier chain. The cryogenic line attenuation is calibrated using the Stark shift method discussed prior, from which we extract the microwave power on the MXC stage of the dilution refrigerator. The power ratio between the thermal noise and the calibration tone detected at room temperature then identifies the magnitude of the thermal

microwave power emitted by the transducer (see Fig. S10c). As a function of optical power, we find overall a relatively constant thermal emission power of ~ -166 dBm, which would be reduced by any isolation placed between the transducer and the readout resonator.

V. EXPERIMENTAL SETUP

The experimental architecture of microwave-only and optical readout is depicted in Fig. S11. In-phase and quadrature signals modulated at MHz frequencies are generated by a baseband Qblox Qubit Control Module (QCM) and used to drive the qubit following upconversion to the GHz domain by an I-Q mixer and RF local oscillator. The I-Q mixer is calibrated to reject the upper sideband of the composite microwave signal. A similar procedure is used to generate readout pulses with a Qblox Qubit Readout Module (QRM). We use a power combiner to transmit readout and drive signals towards the single feedline of the qubit chip. Using a cryogenic microwave switch, the signals emerging from the qubit chip can be directed towards either the electrical input port of the transducer (via two 20 dB isolators and a circulator) or reflected from the switch towards the HEMT. After reflecting from the transducer microwave port or the switch, the signal is transmitted via a 20 dB circulator and an isolator towards a 4K HEMT and two room temperature amplifiers in series. Amplitude and phase information of the signal is then recovered via I-Q down mixing to baseband frequencies and subsequent demodulation by the numerically-controlled oscillator (NCO) of the QRM. For optical readout, the generation of microwave readout signals is identical to the procedure described for microwave-only readout, the only difference being that the RF local oscillator simultaneously drives an EOM in the local oscillator branch of a balanced optical heterodyne detection scheme, which downconverts GHz modulated optical signals to baseband frequencies. An acousto-optic modulator (AOM) is used to pulse the transducer optical pump and turn it on during the readout pulse. Using a custom detection circuit, in-phase and quadrature signals are extracted and demodulated by the NCO of the QRM.

[1] M. J. Weaver, P. Duivestein, A. C. Bernasconi, S. Scharmer, M. Lemang, T. C. van Thiel, F. Hijazi, B. Hensen, S. Gröblacher, and R. Stockill, An integrated microwave-to-optics interface

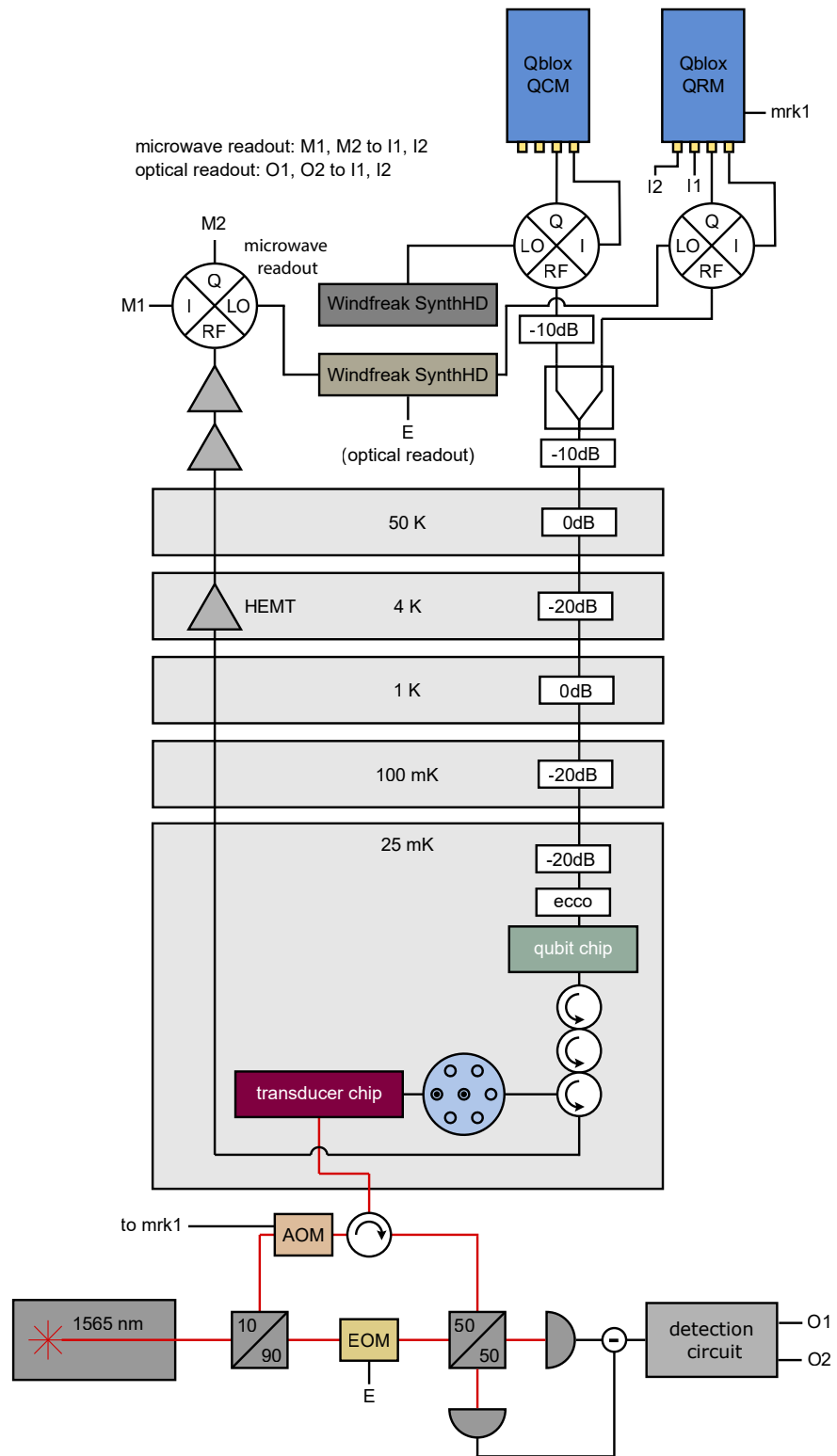


FIG. S11. Microwave and optical wiring. Wiring diagram for microwave-only and optical qubit readout.

- for scalable quantum computing, *Nat. Nanotechnol.* (2023).
- [2] M. Xu, X. Han, W. Fu, C.-L. Zou, and H. X. Tang, Frequency-tunable high-Q superconducting resonators via wireless control of nonlinear kinetic inductance, *Appl. Phys. Lett.* **114**, 192601 (2019).
- [3] I. Rodrigues, D. Bothner, and G. Steele, Coupling microwave photons to a mechanical resonator using quantum interference, *Nat. Commun.* **10**, 5359 (2019).
- [4] R. W. Andrews, R. W. Peterson, T. P. Purdy, K. Cicak, R. W. Simmonds, C. A. Regal, and K. W. Lehnert, Bidirectional and efficient conversion between microwave and optical light, *Nat. Phys.* **10**, 321 (2014).
- [5] D. Schuster, A. Wallraff, A. Blais, L. Frunzio, R.-S. Huang, J. Majer, S. Girvin, and R. Schoelkopf, ac stark shift and dephasing of a superconducting qubit strongly coupled to a cavity field, *Phys. Rev. Lett.* **94**, 123602 (2005).
- [6] M. Aspelmeyer, T. J. Kippenberg, and F. Marquardt, Cavity optomechanics, *Rev. Mod. Phys.* **86**, 1391 (2014).
- [7] M. Kalaei, M. Mirhosseini, P. B. Dieterle, M. Peruzzo, J. M. Fink, and O. Painter, Quantum electromechanics of a hypersonic crystal, *Nat. Nanotechnol.* **14**, 334 (2019).
- [8] A. Yariv, *Optical Electronics in Modern Communications*, 6th ed. (Oxford University Press, 2007) Chap. 9, p. 424.
- [9] S. Schlör, J. Lisenfeld, C. Müller, A. Bilmes, A. Schneider, D. P. Pappas, A. V. Ustinov, and M. Weides, Correlating decoherence in transmon qubits: Low frequency noise by single fluctuators, *Phys. Rev. Lett.* **123**, 190502 (2019).